Chemical Engineering Journal 361 (2019) 304–313

Contents lists available at ScienceDirect

Chemical Engineering Journal

journal homepage: www.elsevier.com/locate/cej

The adsorption characteristics of As_2O_3, Pb^0, PbO and $PbCl_2$ on single atom iron adsorbent with graphene-based substrates

Weijie Yang[a], Zhengyang Gao[a,*], Xiaoshuo Liu[a], Xunlei Ding[b,*], Weiping Yan[a]

[a] School of Energy and Power Engineering, North China Electric Power University, Baoding 071003, China
[b] School of Mathematics and Physics, North China Electric Power University, Beijing 102206, China

HIGHLIGHTS

- Single atom iron catalyst for simultaneous removal of arsenic and lead.
- The adsorption mechanism of As_2O_3, Pb^0, PbO and $PbCl_2$.
- The effect of temperature and competitive adsorption with Hg^0.

GRAPHICAL ABSTRACT

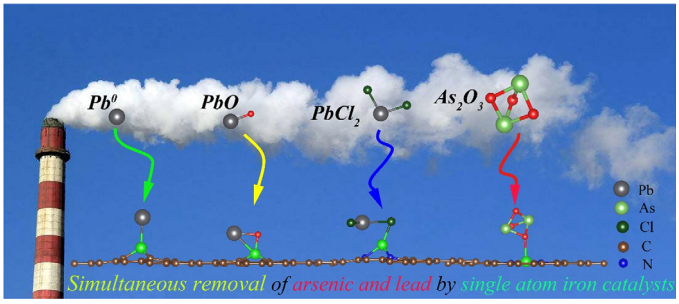

ARTICLE INFO

Keywords:
Arsenic
Lead
Adsorption characteristic
Single atom catalyst
Density functional theory

ABSTRACT

Arsenic and lead released from coal-fired power plant have caused great damage to environment and human health, making it critical to remove arsenic and lead simultaneously. The adsorption characteristics of HTMs (As_2O_3, Pb^0, PbO and $PbCl_2$) on the surface of single atom iron adsorbents supported with graphene-based substrates (Fe/GS) were systematically investigated through density functional theory calculation. The magnetic properties, bonding mechanism, reaction temperature and competitive adsorption behaviors were all considered in this work. Results demonstrated that Fe/GS of single vacancy with three nitrogen atoms doping (Fe/SV-N3) shows the most excellent adsorption capacity for HTMs among four types of Fe/GS. The adsorption of HTMs on Fe/SV-N3 belongs to stable chemisorption, and the adsorption can take place spontaneously when the temperature is below 700 K. To compare with the previously studied Hg^0 system, the competitive adsorption behaviors of Hg^0 and HTMs on Fe/SV-N3 were studied through relative adsorption ratio, Fe/SV-N3 will preferentially adsorb Pb^0 and PbO when Hg^0 and HTMs occur simultaneously at the temperature range of 300–1000 K. Therefore, Fe/SV-N3 is suggested to be a potential new material for gas detection and simultaneous removal of pollutants from coal-fired power plants.

1. Introduction

Hazardous trace elements (HTEs), such as mercury (Hg), arsenic (As) and lead (Pb), released from coal-fired power plant have attracted increasing attention, due to their high toxicity, persistence and bioaccumulation [1]. Although the content of HTEs in coal is low and the air pollution control devices (selective catalytic reduction, electrostatic precipitator, fabric filter and wet flue gas desulfurization) can control HTEs emission effectively, there is still a large amount of HTEs discharged into the atmosphere in light of the huge amount of coal

* Corresponding authors.
E-mail addresses: gaozhyan@163.com (Z. Gao), dingxl@ncepu.edu.cn (X. Ding).

https://doi.org/10.1016/j.cej.2018.12.087
Received 31 October 2018; Received in revised form 15 December 2018; Accepted 17 December 2018
Available online 18 December 2018
1385-8947/

consumption. According to the research of Zhao et al. [2,3], in a 350 MW coal-fired power plant, the concentration of Hg, As and Pb emitted to the atmosphere with all of the existing air pollution control devices were 1.79–2.56 μg/m^3, 0.11–0.25 mg/m^3 and 0.18–0.26 mg/m^3, respectively. According to the data of China statistical yearbook [4], the coal consumption of China in 2017 is 2.69 billion ton, so the emission of Hg, As and Pb to the atmosphere could be 468.76, 38.79 and 47.41 ton, respectively. Noted that the maximum allowable concentrations in residential atmosphere of Hg, As and Pb are 0.0003, 0.003 and 0.0007 mg/m^3, respectively, and even trace amounts of HTEs can cause great harm to the human body [5]. Therefore, the emission pollution of Hg, As and Pb released from coal-fired power plant must be controlled effectively due to their emission amount and toxicity.

It is a consensus that elemental mercury (Hg^0), oxidized mercury (Hg^{2+}) and particulate mercury (Hg^p) are the main forms of mercury in coal-fired flue gas, and the removal of Hg^0 is most difficult due to its high volatility and water-insolubility [6–10]. For arsenic, there may be many components in coal-fired flue gas under different temperature. AsO(g) is the main form of arsenic when temperature is higher than 1000 K. As_2O_5(s) and AsO(g) are the two main forms of arsenic in the temperature range of 650–1000 K [11–13]. While As_2O_3(g) and As_2O_5(s) are the main form of arsenic in the temperature of 750–800 K and 650–700 K, respectively [11–13]. As_2O_3(g) is difficult to be removed by the current air pollution control devices for it high toxicity and water-insolubility, so As_2O_3(g) has been recognized as the main removal object by many researchers [11–15]. For lead, the lead species can be divided into gaseous lead and particulate lead. The gaseous lead contains elemental lead (Pb^0), lead oxide (PbO) and lead dichloride ($PbCl_2$) [16–19], which cannot be directly removed by wet flue gas desulfurization due to their low water-solubility. Therefore, the removal of Hg^0, As_2O_3, Pb^0, PbO and $PbCl_2$ can effectively contribute to control the emission of hazardous trace elements.

Currently, the adsorption and oxidation are two main technology roadmaps for Hg and As, while the adsorption seems to be the main way for Pb [11–13,15,20–30]. It was found that CaO has high adsorption capacity for Hg [31,32], As [15] and Pb [19]. Al_2O_3 and Fe_2O_3 both have removal effect on Hg [33–35], As [15], and Pb [36]. In addition, V_2O_5 [37,38] and MnO_2 [6,7,39] have the catalytic oxidation effect of Hg^0 to Hg^{2+}. Moreover, H_2O_2 [13], $Na_2S_2O_8$ [12], and NaClO [11] can oxidize As_2O_3 to As_2O_5. Although these methods could remove Hg, As and Pb effectively, it is uneconomical to install separate equipment for removing Hg, As and Pb. Simultaneous removal of multiple pollutants (NO_x, SO_2, soot and HTEs) has been the mainstream trend of pollutants removal in coal-fired power plants, which can simplify process and equipment, reduce floor area and improve the operation economy [40–46].

According to our previous studies [47–50], single atom iron doped in graphene-based substrates (Fe/GS) was proposed to be a candidate for the simultaneous removal of multiple pollutants in coal-fired power plant. Specifically, Fe/GS has high catalytic oxidation capacity of NO to NO_2, with only 0.04 eV activation energy [47]. Moreover, Fe/GS has high adsorption capacity for mercury species, and the adsorption of Hg^0 on the surface of Fe/SG belongs to chemical adsorption [48]. In addition, Fe/GS was usually synthetized after calcination at a high temperature of over 800 °C and acid etching [51–56], and it has high thermal stability and chemical stability, indicating that Fe/GS should be regenerated after high temperature heating or solvent extraction. The possible workflow of Fe/GS can be first adsorption and then release, like activated carbon adsorbent. Therefore, Fe/GS should have the fundamental property of adsorbent in the view of recycle, economic and environmental protection.

Based on above discussion, we expect that Fe/GS also has high adsorption capacity for removing As and Pb. If Fe/GS has high adsorption capacity for As and Pb, it will greatly contribute to the simultaneous removal of multiple pollutants. However, there was no theoretical or experimental research about removal of As and Pb by Fe/GS thus far. Therefore, it is necessary to study adsorption mechanism of As_2O_3, Pb^0, PbO and $PbCl_2$ on the surface of Fe/GS at the theoretical level, so as to explore the application possibility of Fe/GS in the removal of As and Pb. Given that As_2O_3, Pb^0, PbO and $PbCl_2$ were all hazardous trace materials (HTMs), those were called by a unified name of HTMs in the next content.

Density functional theory (DFT) has been proved to be a reliable research method for the theoretical study of adsorption and reaction [26,57]. In this work, the adsorption mechanisms of HTMs on Fe/GS were systematically investigated through DFT calculation. Firstly, the most stable adsorption configurations of HTMs on Fe/GS were obtained through optimizing the possible initial adsorption configurations, and some geometric, electric and magnetic properties were summarized. Secondly, the application of magnetic moment variation in gas detection was discussed. Furthermore, projected density of states (PDOS) and Fermi softness analysis were performed to study the difference of adsorption energy and reveal the bonding mechanism. Additionally, the effect of temperature on adsorption energy was discussed through calculating Gibbs free energy. Moreover, the relative adsorption ratios under different temperature were calculated to study the competitive adsorption behaviors of Hg^0 and HTMs.

2. Method

2.1. Calculation method

All DFT calculations were performed based on Perdew–Burke–Ernzerhof (PBE) of generalized gradient approximation (GGA) method and projector augmented wave (PAW) basis set [58–61]. In detail, all calculations were performed in the Vienna ab initio simulation package (VASP). The spin polarization and Van Der Waals interactions were taken into account to acquire the accurate system energy, and the DFT-D3 correction was adopted to describe the weak intermolecular interaction [62]. Consistent with our previous studies [47–50,63], the research model of Fe/GS was built as a 4 × 4 supercell graphene with a 15 Å vacuum layer.

According to our pervious tests [48,49], the kinetic energy cutoff and the width of Gaussian smearing were chosen as 500 eV and 0.05 eV, respectively. In geometry optimization, all atoms were allowed to fully relax with force convergence standard of 0.02 eV/Å and energy convergence standard of 10^{-5} eV. In detail, a 7 × 7 × 1 Γ-centered k-point grid was used to sample the Brillouin zone, which is in agreement with our pervious researches [47–50,63]. In the calculation of system energy, density of states (DOS) and Bader charge, a 15 × 15 × 1 Γ-centered k-point grid was adopted to obtain more accurate energy and detailed electronic structure information.

The stability of catalyst is a key issue. The binding energy (E_b), which can be used to describe the binding strength between graphene-based substrate and Fe atom, was calculated from the following equation:

$$E_b = E_{Fe/GS} - E_{sub} - E_{Fe} \quad (1)$$

where E_{sub}, E_{Fe} and $E_{Fe/GS}$ are the energy of graphene-based substrate, Fe atom and Fe/GS, respectively. To describe the adsorption strength of HTMs (As_2O_3, Pb, PbO and $PbCl_2$) on Fe/GS, the adsorption energy (E_{ads}) was calculated from the following equation:

$$E_{ads} = E_{HTMs\text{-}Fe/g} - E_{Fe/GS} - E_{HTMs} \quad (2)$$

where $E_{HTMs\text{-}Fe/GS}$, $E_{Fe/GS}$ and E_{HTMs} are the energy of adsorption systems, Fe/GS and HTMs (As_2O_3, Pb, PbO and $PbCl_2$), respectively. The energies of HTMs (As_2O_3, Pb^0, PbO and $PbCl_2$) and Fe atom were calculated in a 9.84 Å × 9.84 Å × 15 Å large cell with only Γ point. In detail, the zero-point energy correction was considered in the calculation of adsorption energy.

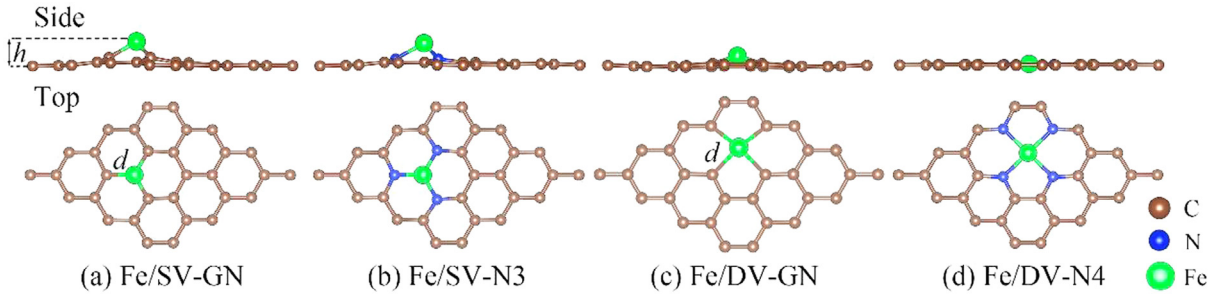

Fig. 1. The geometric structures of Fe/GS.

Table 1
The bond length of C—Fe or N—Fe (d, Å), adsorption height of Fe atom (h, Å), charge of Fe atom (Q, e), magnetic moment (M, μB) and binding energy (E_b, eV) for Fe/GS.

Fe/GS	d (Å)	h (Å)	Q (e)	M (μB)	E_b (eV)
Fe/SV-GN	1.76 (1.76[48])	1.35 (1.36[66])	+0.69	0.00 (0.00[66])	−7.14 (−7.28[67])
Fe/SV-N3	1.78 (1.78[48])	1.23 (1.23[48])	+0.90	3.12	−4.41 (−4.41[49])
Fe/DV-GN	1.86 (1.86[48])	0.66 (0.67[66])	+0.90	2.20 (2.40[68])	−6.12 (−6.47[67])
Fe/DV-N4	1.89 (1.89[48])	0.05 (0.03[69])	+1.08	2.00 (2.00[68])	−7.14 (−7.07[70])

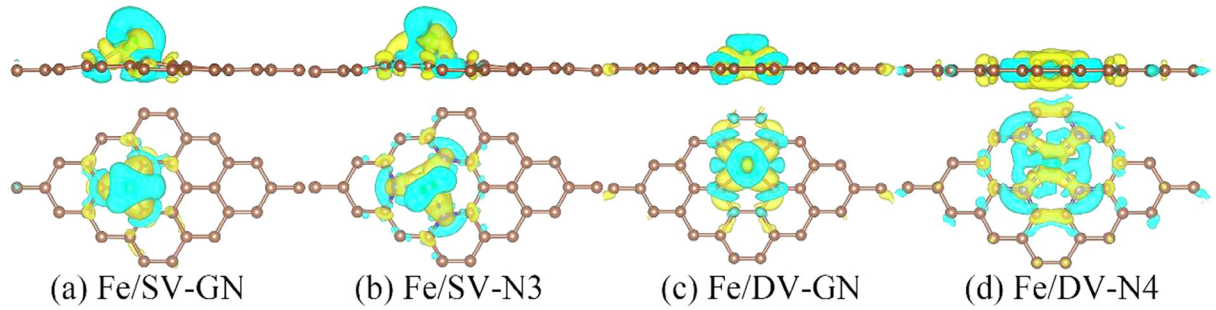

Fig. 2. The charge density difference of Fe/GS. (Contour lines in plots were drawn at 0.003 e/Å^3 intervals; yellow represents accumulation and cyan represents reduction.) (For interpretation of the references to color in this figure legend, the reader is referred to the web version of this article.)

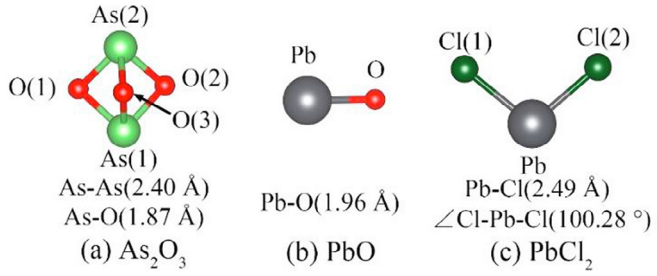

Fig. 3. The geometric structures of As_2O_3, PbO and $PbCl_2$.

2.2. Research model

Vacancy defects and doping nitrogen atoms are two accessible and common methods of graphene modification, hence, four different kinds of Fe/GS were constructed to systematically investigate the performance of Fe/GS with different graphene-based substrates on removing HTMs. In detail, the four kinds of Fe/GS are single vacancy graphene-based substrate (Fe/SV-GN), single vacancy graphene-based substrate with three nitrogen atoms doping (Fe/SV-N3), two vacancies graphene-based substrate (Fe/DV-GN) and two vacancies graphene-based substrate with four nitrogen atoms doping (Fe/DV-N4). The optimized geometric structures and structural information of Fe/GS were shown in Fig. 1 and Table 1, respectively. From Table 1, the calculated results are in good agreement with previous studies, which can guarantee the validity of this work and lay a foundation for the next adsorption study. Compared with the adsorption energy of Fe atom on perfect graphene (1.04 eV) [64] and cohesive energy of Fe (4.28 eV) [65], the adsorption energies of Fe/GS are all large enough to anchor Fe atom firmly. From Fig. 1(a)–(d), the adsorption heights of Fe atom gradually decrease, and the Fe atom of Fe/DV-N4 can be considered as anchored in the plane of graphene-based substrate. To further investigate the electron transfer in the loading process of Fe atom, the charge density difference of Fe/GS was plotted in Fig. 2. From Fig. 2,

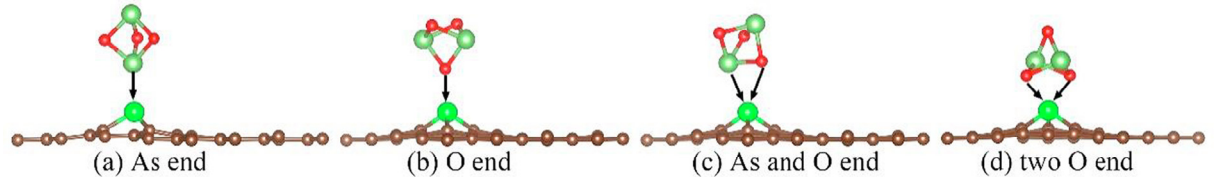

Fig. 4. Four possible adsorption configurations of As_2O_3 on Fe/GS.

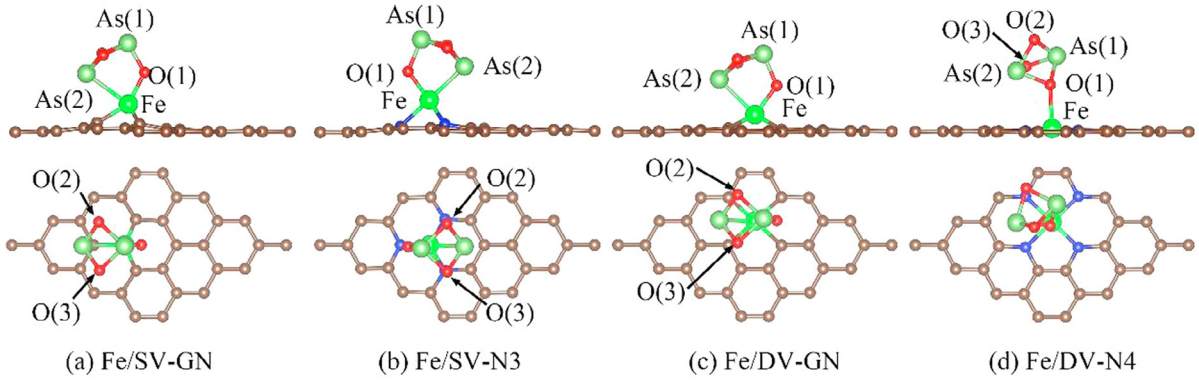

Fig. 5. The most stable adsorption configurations of As_2O_3 on four types of Fe/GS.

Table 2
The bond length, electron transfer (Δq), magnetic moment (M, μB) and adsorption energy (E_{ads}) of As_2O_3. (The symbol of "+" and"–" represents gain and lose electron in electron transfer.)

Properties	Fe/SV-GN	Fe/SV-N3	Fe/DV-GN	Fe/DV-N4
Fe—O(1) (Å)	1.85	1.84	1.87	2.27
O(1)—As(1) (Å)	1.74	1.79	1.78	1.89
As(1)—O(2) (Å)	1.90	1.86	1.87	1.89 (O(1)—As(2) (Å))
As(1)—O(3) (Å)	1.90	1.87	1.87	1.86 (As(1)—O(2) (Å))
As(2)—O(2) (Å)	1.81	1.85	1.84	1.86 (As(1)—O(3) (Å))
As(2)—O(3) (Å)	1.81	1.85	1.84	1.88 (As(2)—O(2) (Å))
As(2)—Fe (Å)	2.69	2.52	2.60	1.87 (As(2)—O(3) (Å))
Δq-As_2O_3 (e)	+0.26	+0.55	+0.34	−0.04
Δq-Fe (e)	−0.13	−0.08	−0.03	−0.04
Δq-Gra (e)	−0.13	−0.47	−0.31	+0.08
M (μB)	0.00	0.91	1.07	2.00
E_{ads} (eV)	−1.91	−2.20	−1.46	−0.21

the reduction of charge density occurred at the vicinity of Fe and its neighboring C atoms, and the accumulation of charge density happened near the Fe—C bond. This obvious electron transfer phenomenon indicates that a stable chemical bond was formed between Fe atom and its neighboring C atoms, which can further testify the stability of Fe/GS.

According to the research of da Hora et al. [71], the most stable structure of As_2O_3 was the type of D3H. The optimized geometric structures and structure information of As_2O_3, PbO and $PbCl_2$ were shown in Fig. 3. The bond lengths of As—As and As—O were 2.40 Å and 1.87 Å, which are consistent with the number reported by da Hora et al (2.40 Å and 1.84 Å) [71]. For PbO, the bond length of Pb—O (1.96 Å) is consistent with the experimental data (1.92 Å) [72]. For $PbCl_2$, the bond length of $PbCl_2$ (2.49 Å) and bond angle of $PbCl_2$ (100.28°) are all consistent with a previous study (2.55 Å and 100.3°) [73].

3. Results and discussion

3.1. Adsorption of As_2O_3

To acquire the most stable adsorption configuration of As_2O_3, four possible adsorption configurations were considered, as shown in Fig. 4. The most stable adsorption configurations of As_2O_3 on each type of Fe/GS were obtained based on the above four possible adsorption configurations, as shown in Fig. 5.

Table 3
The bond length, distance between Pb and graphene plane (Δh-Pb), electron transfer (Δq), magnetic moment (M, μB) and adsorption energy (E_{ads}) of Pb^0. (The symbol of "+" and"–" represents gain and lose electron in electron transfer.)

Properties	Fe/SV-GN	Fe/SV-N3	Fe/DV-GN	Fe/DV-N4
Fe—Pb (Å)	2.60	2.41	2.51	2.37
Δh-Pb (Å)	3.94	3.86	2.08	2.86
Δq-Pb (e)	−0.17	−0.07	−0.75	−0.41
Δq-Fe (e)	+0.13	+0.21	+0.15	+0.34
Δq-Gra (e)	+0.04	−0.14	+0.60	+0.07
M (μB)	0.28	1.43	2.14	0.00
E_{ads} (eV)	−1.55	−2.15	−2.90	−1.95

From Fig. 5, the most stable adsorption configurations of As_2O_3 all exist in the bonding form of Fe—O bond. Expect for Fe/DV-N4, dissociation adsorption is the most stable adsorption form of As_2O_3 on Fe/GS, which is similar to the adsorption of As_2O_3 on carbonaceous surface [57]. In addition, some important parameters (bond length, electron transfer and adsorption energy) were summarized in Table 2. Because the adsorption configuration of As_2O_3 on Fe/DV-N4 was different from others, some special bond lengths were listed in the fifth column of Table 2. With regards to the adsorption of As_2O_3 on the surface of Fe/SV-GN, Fe/SV-N3 and Fe/DV-GN, As_2O_3 gained electron, while Fe atom and graphene-based substrates lost electron. However, graphene-based substrates gained electron, while As_2O_3 and Fe atom lost electron in the adsorption of As_2O_3 on the surface of Fe/DV-N4. Accordingly, the adsorption of As_2O_3 on the surface of Fe/SV-GN, Fe/SV-N3 and Fe/DV-GN all belong to stable chemisorption, and the adsorption of As_2O_3 on Fe/DV-N4 belongs to weak physisorption. In detail, the adsorption of As_2O_3 on Fe/SV-N3 is the strongest among four kinds of Fe/GS with an adsorption energy of −2.09 eV. According to the adsorption energies of As_2O_3, we can conclude that Fe/GS (expect for Fe/DV-N4) seems to be a promising adsorbent for removing As_2O_3.

3.2. Adsorption of Pb^0

The optimized adsorption configurations of Pb^0 on the surface of Fe/GS were shown in Fig. 6, and some important parameters in

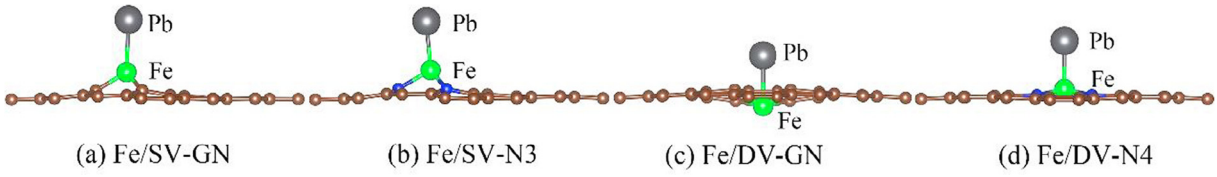

Fig. 6. The most stable adsorption configurations of Pb^0 on four types of Fe/GS.

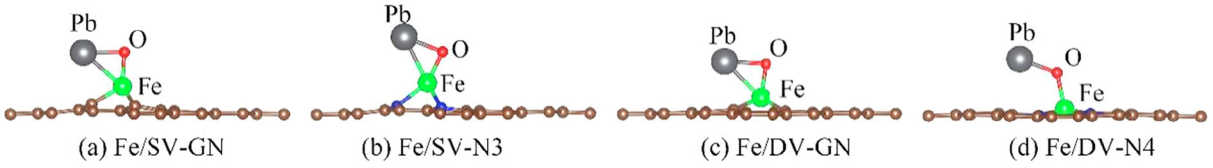

Fig. 7. The most stable adsorption configurations of PbO on four types of Fe/GS.

Table 4
The bond length, electron transfer (Δ*q*), magnetic moment (*M*, μB) and adsorption energy (E_{ads}) of PbO. (The symbol of "+" and"–" represents gain and lose electron in electron transfer.)

Properties	Fe/SV-GN	Fe/SV-N3	Fe/DV-GN	Fe/DV-N4
Fe—O (Å)	1.78	1.79	1.77	1.92
Pb—O (Å)	2.13	2.14	2.17	2.06
Fe—Pb (Å)	2.68	2.67	2.66	3.48
∠Pb—O—Fe (°)	85.86	85.12	84.63	121.95
Δq-PbO (e)	0.00	0.35	−0.11	0.08
Δq-Fe (e)	−0.14	−0.10	−0.01	−0.14
Δq-Gra (e)	0.14	−0.25	0.12	0.06
M (μB)	0.00	3.05	1.18	2.00
E_{ads} (eV)	−2.68	−2.83	−2.21	−0.91

Table 5
The bond length, electron transfer (Δ*q*), magnetic moment (*M*, μB) and adsorption energy (E_{ads}) of $PbCl_2$. (The symbol of "+" and"–" represents gain and lose electron in electron transfer.)

Properties	Fe/SV-GN	Fe/SV-N3	Fe/DV-GN	Fe/DV-N4
Fe—Cl(1) (Å)	2.23	2.26	2.28	3.10 (Fe—Pb (Å))
Pb—Cl(1) (Å)	2.74	2.72	2.70	2.54
Pb—Cl(2) (Å)	2.50	2.53	2.51	2.54
∠Cl—Pb—Cl (°)	96.62	99.91	96.06	99.05
Δ*q*-$PbCl_2$ (e)	+0.02	+0.28	+0.01	+0.18
Δ*q*-Fe (e)	−0.05	−0.04	−0.01	+0.12
Δ*q*-Gra (e)	+0.03	−0.24	0.00	−0.30
M (μB)	0.00	3.12	1.68	1.80
E_{ads} (eV)	−1.53	−1.89	−1.12	−0.43

adsorption process were summarized in Table 3. In the adsorption process of Pb^0, there is obvious electron transfer between Pb atom and Fe/GS. Pb^0 always lost electron while Fe atom always gained electron in the adsorption of Pb^0. According to the value of adsorption energy, the adsorption of Pb^0 on the surface of Fe/GS all belongs to strong chemisorption. Fe/DV-GN has the strongest adsorption capacity for Pb^0 with an adsorption energy of −2.93 eV, which may be related to its unique adsorption configuration and the largest amount of electron transfer (0.75 e). According to previous theoretical and experimental studies [74–76], the metal dimer supported with graphene-based substrates can obviously improve the catalytic activity of catalysts. In the adsorption of Pb^0 on Fe/GS, it is noteworthy that there is a Fe-Pb dimer formed in configure of Fig. 6c, with a 2.08 Å distance between Pb and graphene plane. The atomic radii of C and Pb are 0.67 and 1.54 Å [77], and the distance between Pb and graphene plane is smaller than the sum of atomic radii of C and Pb, which can further confirm the formation of Fe-Pb dimer.

3.3. Adsorption of PbO

The optimized adsorption configurations of PbO on the surface of Fe/GS were shown in Fig. 7, and some important parameters in the process of adsorption were summarized in Table 4. Compared with the bond length of gaseous PbO (1.96 Å), the bond lengths of adsorbed PbO were all obviously elongated, which may indicate that there is a strong interaction between PbO and Fe/GS. From Table 4, the adsorption of PbO on Fe/GS belongs to chemical adsorption according to the adsorption energy of PbO. In detail, Fe/SV-N3 has the strongest adsorption capacity for PbO, with an adsorption energy of −2.75 eV.

3.4. Adsorption of $PbCl_2$

The optimized adsorption configurations of $PbCl_2$ on Fe/GS were shown in Fig. 8, and some important parameters in the process of adsorption were summarized in Table 5. From Fig. 8, the most stable adsorption configurations of $PbCl_2$ on Fe/SV-GN, Fe/SV-N3 and Fe/DV-GN all exist in the bonding form of Fe—Cl bond, while that of Fe/DV-N4

Table 6
The variation of magnetic moment after adsorption. (The symbol of "+" and"–" represents gain and lose electron in magnetic moment.)

Δ*M*(μB)	Fe/SV-GN	Fe/SV-N3	Fe/DV-GN	Fe/DV-N4
As_2O_3	0	−2.21	−1.13	0
Pb^0	+0.28	−1.69	−0.06	−2.00
PbO	0	−0.07	−1.02	0
$PbCl_2$	0	0	−0.52	−0.20

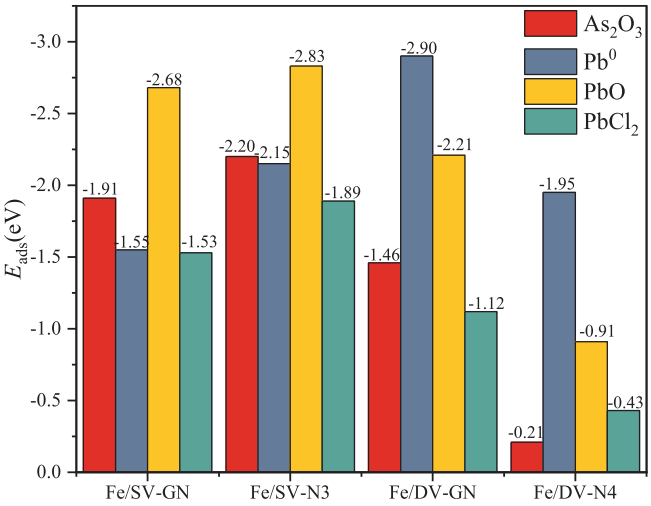

Fig. 9. The adsorption energies of As_2O_3, Pb^0, PbO and $PbCl_2$ on Fe/GS.

Fig. 8. The most stable adsorption configurations of $PbCl_2$ on four types of Fe/GS.

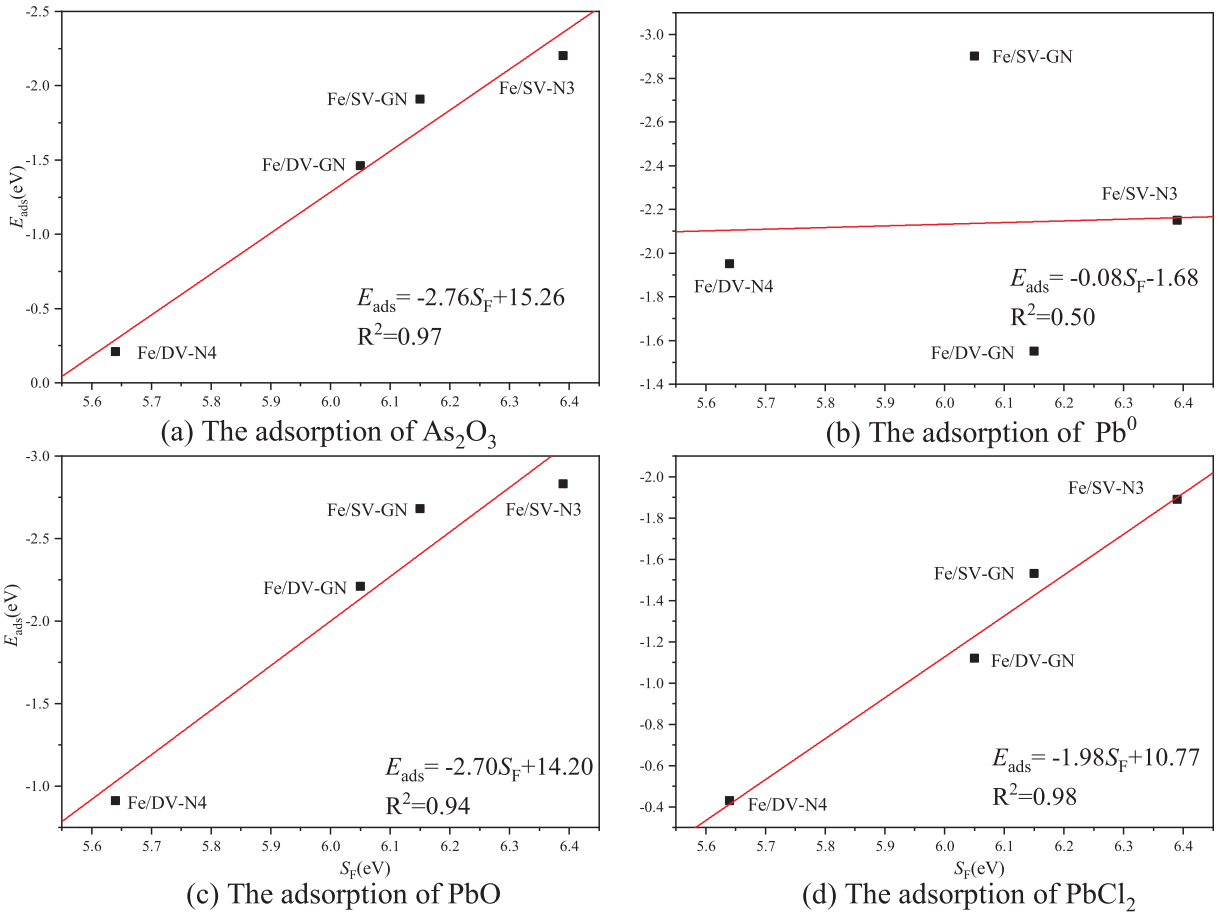

Fig. 10. The adsorption energy of As_2O_3, Pb^0, PbO and $PbCl_2$ as a function of Fermi softness.

is in the Fe—Pb bonding form. From Table 5, $PbCl_2$ always gained electron in the adsorption process of $PbCl_2$. According to the number of adsorption energy, the adsorptions of $PbCl_2$ on the surface of Fe/SV-GN, Fe/SV-N3 and Fe/DV-GN all belong to chemisorption, while the adsorption of $PbCl_2$ on Fe/DV-N4 belongs to physisorption. Similar to the adsorption of PbO on the surface of Fe/GS, the adsorption strength order of $PbCl_2$ on Fe/GS is Fe/SV-N3 > Fe/SV-GN > Fe/DV-GN > Fe/DV-N4.

3.5. Analysis of magnetic moment

According to the research of Tang et al. [78], the variation of magnetic moment can provide the theoretical guide for the design of gas sensors. Therefore, the variations of magnetic moment (ΔM) after adsorption were summarized in Table 6. From Table 6, the magnetic moment either remains constant or reduces after adsorption, and the variation of magnetic moment is positive only in the adsorption system of Pb^0 on Fe/SV-GN. In the adsorption system of HTMs on Fe/SV-GN, the ΔM of As_2O_3, PbO and $PbCl_2$ are zero, while the ΔM of Pb^0 is different from others (+0.28 μB), suggesting that Fe/SV-GN is a candidate for Pb^0 detection in a mixed atmosphere of As_2O_3, Pb^0, PbO and $PbCl_2$. Similar to Fe/SV-GN, the ΔM of $PbCl_2$ on Fe/SV-N3 is zero, which is different from others in the adsorption system of HTMs, indicating that Fe/SV-N3 is a potential candidate for $PbCl_2$ detection in a mixed atmosphere of As_2O_3, Pb^0, PbO and $PbCl_2$.

3.6. Analysis of adsorption energy

In order to clearly compare the adsorption capacity of HTMs on Fe/GS, the values of adsorption energies were plotted in Fig. 9. From Fig. 9, the adsorption energies of As_2O_3, Pb^0, PbO and $PbCl_2$ on Fe/SV-GN and Fe/SV-N3 were all larger than 1.5 eV, suggesting that the two kinds of Fe/GS with single vacancy have strong adsorption capacity for HTMs. Moreover, the adsorption capacity of Fe/SV-N3 is superior to Fe/SV-GN. However, Fe/DV-N4 has strong adsorption capacity only for Pb^0. Combined with the adsorption energies of As_2O_3, Pb^0, PbO and $PbCl_2$, Fe/SV-N3 shows the best removal capacity of HTMs among four types of Fe/GS. Considering the complexity of flue gases, the adsorption energies of various flue gases, such as N_2, O_2, CO, CO_2, NO, N_2O, NO_2, HCl, H_2O, H_2S, NH_3 and SO_2, were calculated to comprehensively study the adsorptive characteristics of adsorbents in various flue gases, and the detailed data of adsorption energies were summarized in Table S1. Among the calculated flue gases, only the adsorption energies of O_2, NO and NO_2 are larger than that of HTMs, which may indicate that the Fe/GS will preferentially adsorb O_2, NO, NO_2 and HTMs in the various flue gases. According to our previous study [47], the adsorbed O_2 and NO will be catalytically oxidized to produce NO_2, so the main adsorbed species should be NO_2 and HTMs. Moreover, based on our previous study [48], the adsorption energy of Hg^0 on Fe/SV-N3 is −0.81 eV, belonging to stable chemisorption. Therefore, Fe/SV-N3 is suggested to be a potential new material for simultaneous removal of NO, Hg^0, arsenic and lead in coal-fired flue gas.

According to our previous studies [48,49], Fermi softness (S_F) proposed by Zhuang [79] can be a good descriptor of adsorption capacity in the system of Fe/GS, so we adopted S_F to explain the difference in adsorption energy of same gas on different catalyst surfaces. Based on our pervious calculation [48], the S_F of Fe/SV-GN, Fe/SV-N3, Fe/DV-GN and Fe/DV-N4 were 6.15, 6.39, 6.05 and 5.64 eV, respectively. Moreover, the linear fitting between E_{ads} and S_F was performed, as shown in Fig. 10. From Fig. 10, the correlation coefficient square (R^2) of

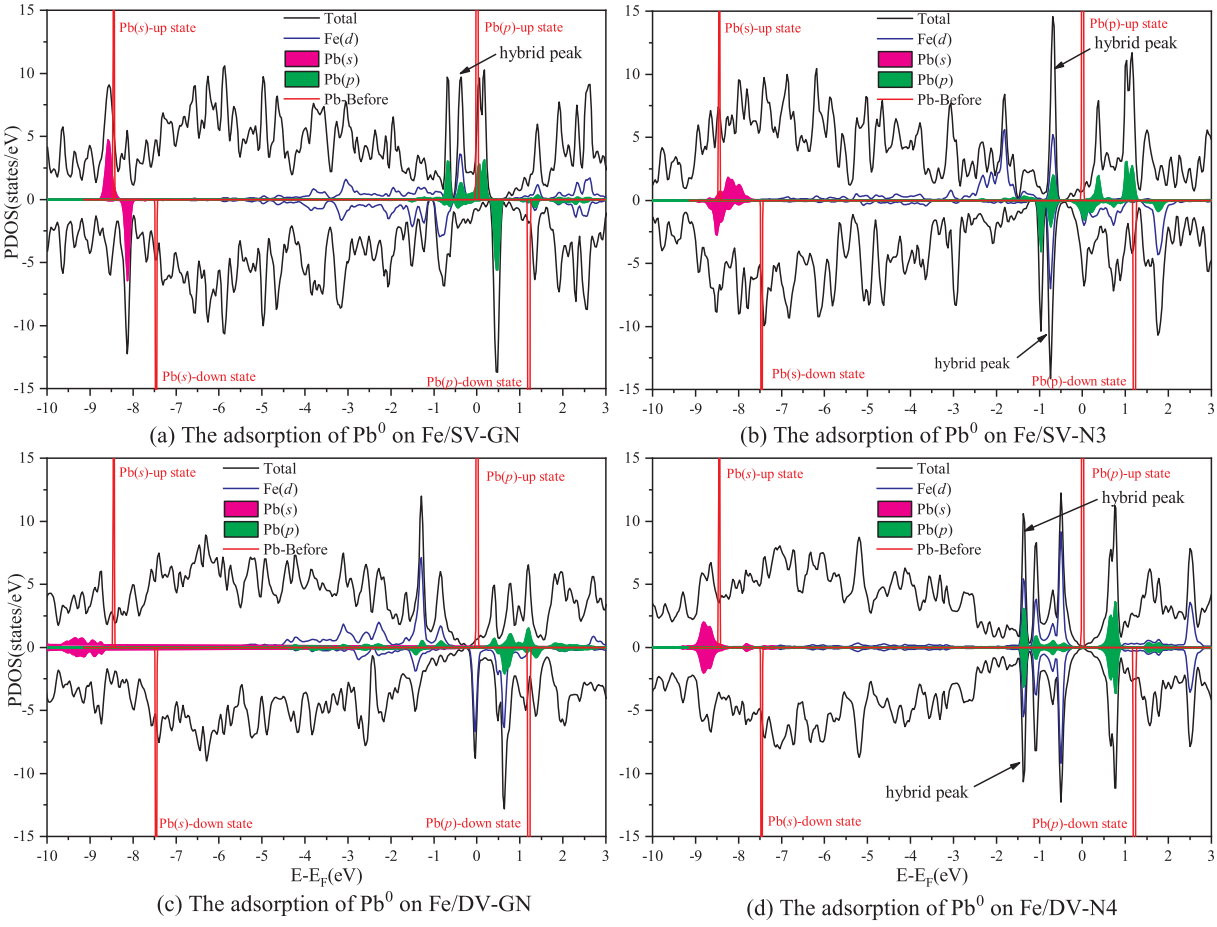

Fig. 11. The PDOS of four different adsorption systems.

E_{ads} and S_F in the adsorption process of As_2O_3, PbO and $PbCl_2$ on Fe/GS were 0.97, 0.94 and 0.98, respectively, suggesting that there was an obvious linear correlation between E_{ads} and S_F in the adsorption system of As_2O_3, PbO and $PbCl_2$. In detail, the order of adsorption capacity should be Fe/SV-N3 > Fe/SV-GN > Fe/DV-GN > Fe/DV-N4 according to the adsorption energies of As_2O_3, PbO and $PbCl_2$. However, a poor linear relationship was found in the adsorption system of Pb^0, which may be related with their electronic structures. To further study the difference of adsorption energy in the adsorption system of on Pb^0, the PDOS of four different adsorption configurations were plotted, as shown in Fig. 11.

In Fig. 11, the total density of states, *d* orbital of Fe, *s* orbital and *p* orbital of Pb in the adsorption system were plotted in black, blue, purple and green color, respectively. The orbital of gaseous Pb before adsorption was plotted in red color. Comparing the *s* and *p* orbitals of adsorbed Pb and gaseous Pb, the *s* and *p* orbitals of Pb shifted down to the lower energy states, suggesting that the adsorption processes of Pb^0 on the surface of Fe/GS are exothermic and stable. Expect for Fe/DV-GN, there were obvious hybrid peaks between the *d* orbital of Fe and the *p* orbital of Pb in map of PDOS, which indicates that hybridization effect contributes to the formation of covalent bond in the adsorption process of Pb^0 on Fe/SV-GN, Fe/SV-N3 and Fe/DV-N4. According to the data of electron transfer in Table 3, there was obvious electron transfer phenomenon in the adsorption system of Pb^0 on Fe/GS, which can suggest that there were formations of ionic bonds in the adsorption process of Pb^0 on Fe/GS. Therefore, we can conclude that the adsorption processes of Pb^0 on Fe/SV-GN, Fe/SV-N3 and Fe/DV-N4 were determined by both covalent and ionic bonds.

In particular, there was no hybrid peak between Fe(*d*) and Pb(*p*) in the adsorption process of Pb^0 on Fe/DV-GN. In Fig. 11(c), the occupied electrons of Pb(*s*) and Pb(*p*) were significantly reduced, which is consistent with the significant electron transfer phenomenon (0.75 e). This obvious electron transfer contributes to a stable ionic bond which is stronger than the other three, and this ionic bond effect should be the origin of largest adsorption energy. Therefore, the adsorption process of Pb^0 on Fe/DV-GN was dominated by strong ionic bond effect. Moreover, there were two hybrid peaks in the adsorption process of Pb^0 on Fe/SV-N3 and Fe/DV-N4, while only one hybrid peak appeared in the adsorption process of Pb^0 on Fe/SV-GN, which can explain that the adsorption energy of Pb^0 on Fe/SV-N3 and Fe/DV-N4 is similar (−2.15 eV and −1.95 eV) and the adsorption energy of Pb^0 on Fe/SV-GN is the smallest (−1.55 eV).

From the above PDOS analysis, the adsorption strength order of Pb^0 on Fe/GS could be understood and the special characteristics of Pb^0 adsorption systems were found. The adsorption system of Pb^0 has strong ionic and covalent bond effect simultaneously. Due to its special bonding mechanism, the phenomenon that S_F showed a poor prediction capacity of adsorption energy in this adsorption system can be understood. Furthermore, it is concluded that S_F may not be applicable to the systems with strong ionic bond and strong covalent bond at the same time.

3.7. The effect of temperature

The temperature has a significant effect on adsorption characteristic, so the adsorption energies were calculated in Gibbs free energy under different reaction temperatures to consider the effect of temperature. In detail, the Gibbs free energies of gas and solid can be obtained according to the next equations:

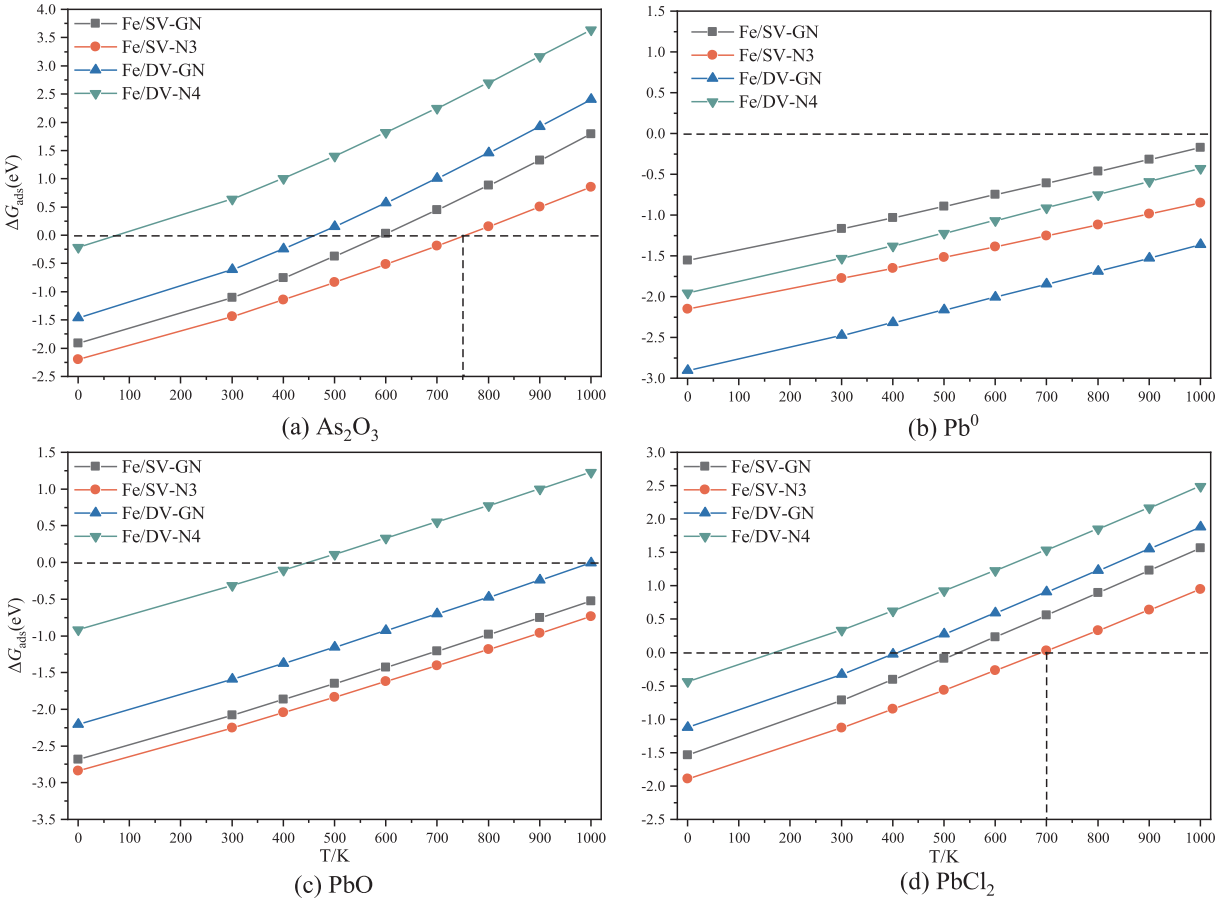

Fig. 12. The ΔG_{ads} of As_2O_3, Pb^0, PbO and $PbCl_2$ on the surface of Fe/GS.

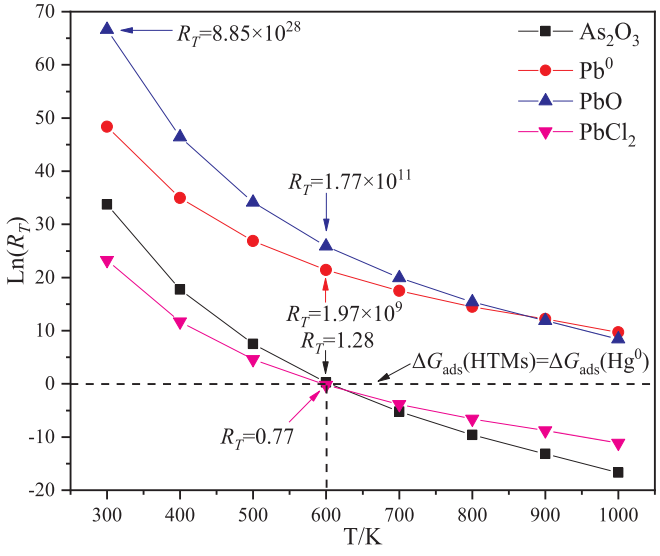

Fig. 13. The natural logarithm of R_T under different temperatures.

$$G_{gas} = E_{ele} + ZPE + RT - TS \quad (3)$$

$$G_{solid} = E_{ele} + ZPE - TS \quad (4)$$

where E_{ele} is the ground-state energy of the system; ZPE is the zero point energy correction which can be acquired from vibrational frequency calculation; R is the gas constant (8.62×10^{-5} eV mol^{-1} K^{-1}); S is the entropy which can also be calculated from vibrational frequency calculation. Therefore, the calculation formula of adsorption energy can be represented by the following equation:

$$\Delta G_{ads} = G_{HTMs\text{-}Fe/GS} - G_{Fe/GS} - G_{HTMs} \quad (5)$$

where $G_{HTMs\text{-}Fe/GS}$, $G_{Fe/GS}$ and G_{HTMs} are the Gibbs free energies of the adsorption system, Fe/GS and HTMs, respectively. In detail, the vibrational frequency calculations were performed through numerical Hessian calculations with finite displacements of ± 0.02 Å [47–50].

According to the temperature level of flue gas in the tail flue of coal-fired power plant, the research temperature range was selected from 300 K to 1000 K. The ΔG_{ads} of As_2O_3, Pb^0, PbO and $PbCl_2$ on Fe/GS were plotted in Fig. 12. From Fig. 12, the higher the temperature, the weaker the adsorption strength, suggesting that the temperature has an obvious inhibition effect on the adsorption strength. In Fig. 12(b), the number of ΔG_{ads} of Pb^0 on Fe/GS was all below zero, which indicates that the adsorption process can take place spontaneously. According to the adsorption characteristic of HTMs on Fe/GS at the range of 300 K–1000 K, Fe/SV-N3 is the most suitable candidate among four different Fe/GS. In detail, the adsorption processes of Pb^0 and PbO on Fe/SV-N3 both can take place spontaneously at the research temperature range. The adsorption processes of As_2O_3 and $PbCl_2$ on Fe/SV-N3 can take place spontaneously when the temperature was below 750 K and 700 K, respectively. Therefore, the working temperature of Fe/SV-N3 for removing As_2O_3, Pb^0, PbO and $PbCl_2$ in coal-fired power plant should be below 700 K.

3.8. The competitive adsorption behavior

To further investigate the adsorption characteristics of As_2O_3, Pb^0, and PbO and $PbCl_2$ on Fe/SV-N3, the relative adsorption ratios (R_T) of As_2O_3, Pb^0, and PbO and $PbCl_2$ were calculated at the temperature range of 300 K–1000 K. To facilitate the discussion, Hg^0 was chosen as

the reference gas to calculate R_T at the standard atmospheric pressure. In actual coal-fired flue gas, the concentration of Hg^0, As_2O_3, Pb^0, and PbO and $PbCl_2$ were all at the level of ppm, so we supposed that the partial pressures of As_2O_3, Pb^0, and PbO and $PbCl_2$ were all equal to that of Hg^0. According to the Boltzmann distribution, R_T was obtained from the following equation:

$$R_T = \frac{N(HTMs)}{N(Hg^0)} = \exp\left(-\frac{\Delta G_{ads}(HTMs) - \Delta G_{ads}(Hg^0)}{k_B T}\right) \quad (6)$$

where ΔG_{ads} is the adsorption energy of HTMs or Hg^0 calculated in Gibbs free energy, k_B is the Boltzmann constant (8.62×10^{-5} eV/K). The data of $\Delta G_{ads}(Hg^0)$ were obtained from our pervious study [48], and the values of $\Delta G_{ads}(Hg^0)$ and R_T were summarized in Table S1 (ESI). In order to observe the variation of R_T conveniently, the natural logarithm of R_T under different temperatures were plotted in Fig. 13.

In Fig. 13, the dotted line indicates that the ΔG_{ads}(HTMs) is equal to $\Delta G_{ads}(Hg^0)$ and the adsorption capacity of HTMs is equal to that of Hg^0 ($R_T = 1$). HTMs will play a dominant role when competitive adsorption between HTMs and Hg^0 occurs above the dotted line. From Fig. 13, the R_T of As_2O_3, Pb^0, PbO and $PbCl_2$ all decreased with the increase of temperature. In detail, the Ln(R_T) of Pb^0 and PbO were all larger than zero, suggesting that the adsorption capacity of Pb^0 and PbO on Fe/GS are both superior to Hg^0 at the research temperature range. However, the adsorption of As_2O_3 and $PbCl_2$ gets the edge only at the temperature range of 300–600 K. Compared with As_2O_3 and $PbCl_2$, the adsorption of Hg^0 on Fe/SV-N3 is dominant when the temperature is above 600 K. Fe/SV-N3 preferentially adsorbs Pb^0 and PbO when Hg^0, As_2O_3, Pb^0, PbO and $PbCl_2$ occur simultaneously at the research temperature range. In practical application, the curve of R_T under different temperature can provide the guide to determine the temperature window of Fe/SV-N3 according to the concentration of pollutant components in coal-fired fuel gas.

4. Conclusion

The adsorption characteristics of As_2O_3, Pb^0, PbO and $PbCl_2$ on Fe/GS were systematically investigated through the analysis of geometric, electric and magnetic properties. According to the variation of magnetic moment, Fe/SV-GN and Fe/SV-N3 are promising gas detectors for Pb^0 and $PbCl_2$ in the mixed atmosphere of As_2O_3, Pb^0, PbO and $PbCl_2$, respectively. Fermi softness may not be applicable to the system which has strong ionic and covalent bond at the same time. Based on the adsorption energy, Fe/SV-N3 showed the most excellent adsorption capacity for As_2O_3, Pb^0, PbO and $PbCl_2$, suggesting that Fe/SV-N3 seems to be a candidate adsorbent for simultaneous removal of As_2O_3, Pb^0, PbO and $PbCl_2$. The temperature has an inhibitory effect on the adsorption, and the adsorption processes of As_2O_3, Pb^0, PbO and $PbCl_2$ can take place spontaneously when the temperature is below 700 K. The competitive adsorption behaviors of Hg^0 and HTMs on Fe/SV-N3 were studied through calculating relative adsorption ratio under different temperatures, Fe/SV-N3 will preferentially adsorb Pb^0 and PbO when Hg^0, As_2O_3, Pb^0, PbO and $PbCl_2$ occur simultaneously at the research temperature range. Based on the above research, we can conclude that Fe/SV-N3 should be a potential new material for simultaneous removal of pollutants from coal-fired power plants.

We hope this theoretical exploration can lay a foundation for related theoretical study and provide a guideline for further experimental investigation. For further study, some experimental investigations would be carried out to study the adsorption characteristic, multicomponent competitive adsorption and temperature effect based on this research. The cycling and regeneration properties of Fe/GS should also be carefully examined. The effect of adsorbed O_2, NO, NO_2 and other flue gases on the adsorption of HTMs on Fe/GS should be investigated. In addition, the adsorption of HTMs on Fe-Pb dimer will be studied in the next theoretical research.

Acknowledgements

This work was supported by the National Natural Science Foundation of China (No. 91545122), Beijing Natural Science Foundation (2182066), Natural Science Foundation of Hebei Province of China (B2018502067) and the Fundamental Research Funds for the Central Universities (2017XS121 and JB2015RCY03). Computational resources from the Lvliang Supercomputer Center were acknowledged.

Appendix A. Supplementary data

Supplementary data to this article can be found online at https://doi.org/10.1016/j.cej.2018.12.087.

References

[1] J.R. Bunt, F.B. Waanders, Trace element behaviour in the Sasol-Lurgi MK IV FBDB gasifier. Part 1 – the volatile elements: Hg, As, Se, Cd and Pb, Fuel 87 (2008) 2374–2387.
[2] S. Zhao, Y. Duan, L. Chen, Y. Li, T. Yao, S. Liu, M. Liu, J. Lu, Study on emission of hazardous trace elements in a 350 MW coal-fired power plant. Part 1. Mercury, Environ. Pollut. 229 (2017) 863–870.
[3] S. Zhao, Y. Duan, L. Chen, Y. Li, T. Yao, S. Liu, M. Liu, J. Lu, Study on emission of hazardous trace elements in a 350 MW coal-fired power plant. Part 2. Arsenic, chromium, barium, manganese, lead, Environ. Pollut. 226 (2017) 404–411.
[4] N.B.o. Statistics, China Statistical Yearbook, China Statistics Press, Beijing, 2017.
[5] M.o.H.o.t.P.s.R.o. China, Hygienic Standards for the Design of Enterprises, in Chinese, People's Medical Publishing House, 2010.
[6] B. Zhang, J. Liu, Y. Yang, M. Chang, Oxidation mechanism of elemental mercury by HCl over MnO_2 catalyst: Insights from first principles, Chem. Eng. J. 280 (2015) 354–362.
[7] B. Zhang, J. Liu, C. Zheng, M. Chang, Theoretical study of mercury species adsorption mechanism on MnO_2(110) surface, Chem. Eng. J. 256 (2014) 93–100.
[8] L. Ling, S. Zhao, P. Han, B. Wang, R. Zhang, M. Fan, Toward predicting the mercury removal by chlorine on the ZnO surface, Chem. Eng. J. 244 (2014) 364–371.
[9] W. Xiang, J. Liu, M. Chang, C. Zheng, The adsorption mechanism of elemental mercury on CuO (110) surface, Chem. Eng. J. 200–202 (2012) 91–96.
[10] M.T. Izquierdo, D. Ballestero, R. Juan, E. Garcia-Diez, B. Rubio, C. Ruiz, M.R. Pino, Tail-end Hg capture on Au/carbon-monolith regenerable sorbents, J. Hazard. Mater. 193 (2011) 304–310.
[11] Y. Zhao, W. Qiu, C. Yang, J. Wang, Removal of arsenic from flue gas by using NaClO solution, Chem. Eng. J. 309 (2017) 1–6.
[12] Y. Zhao, W. Qiu, Arsenic oxidation and removal from flue gas using $H_2O_2/Na_2S_2O_8$ solution, Fuel Process. Technol. 167 (2017) 355–362.
[13] Y. Zhao, W. Qiu, C. Yang, J. Wang, Study on a novel oxidation process for removing arsenic from flue gas, Energy Fuels 31 (2016) 693–698.
[14] Y. Zhang, P. Shang, J. Wang, P. Norris, C.E. Romero, W.-P. Pan, Trace element (Hg, As, Cr, Cd, Pb) distribution and speciation in coal-fired power plants, Fuel 208 (2017) 647–654.
[15] Y. Zhang, C. Wang, W. Li, H. Liu, Y. Zhang, P. Hack, W. Pan, Removal of gas-phase As_2O_3 by metal oxide adsorbents: effects of experimental conditions and evaluation of adsorption mechanism, Energy Fuels 29 (2015) 6578–6585.
[16] R. Yoshiie, Y. Taya, T. Ichiyanagi, Y. Ueki, I. Naruse, Emissions of particles and trace elements from coal gasification, Fuel 108 (2013) 67–72.
[17] W. Song, F. Jiao, N. Yamada, Y. Ninomiya, Z. Zhu, Condensation behavior of heavy metals during oxy-fuel combustion: deposition, species distribution, and their particle characteristics, Energy Fuels 27 (2013) 5640–5652.
[18] W.P. Linak, J.O.L. Wendt, Trace metal transformation mechanisms during coal combustion, Fuel Process. Technol. 39 (1994) 173–198.
[19] M. Uberoi, F. Shadman, Sorbents for removal of Lead compounds from hot flue gases, AIChE J. 36 (1990) 307–309.
[20] W. Chen, Y. Pei, W. Huang, Z. Qu, X. Hu, N. Yan, Novel effective catalyst for elemental mercury removal from coal-fired flue gas and the mechanism investigation, Environ. Sci. Technol. 50 (2016) 2564–2572.
[21] L. Zhao, C. Li, X. Zhang, G. Zeng, J. Zhang, Y.e. Xie, A review on oxidation of elemental mercury from coal-fired flue gas with selective catalytic reduction catalysts, Catal. Sci. Technol. 5 (2015) 3459–3472.
[22] Y. Gao, Z. Zhang, J. Wu, L. Duan, A. Umar, L. Sun, Z. Guo, Q. Wang, A critical review on the heterogeneous catalytic oxidation of elemental mercury in flue gases, Environ. Sci. Technol. 47 (2013) 10813–10823.
[23] L. Tong, T. Yue, P. Zuo, X. Zhang, C. Wang, J. Gao, K. Wang, Effect of characteristics of KI-impregnated activated carbon and flue gas components on Hg^0 removal, Fuel 197 (2017) 1–7.
[24] B. Zhao, H. Yi, X. Tang, Q. Li, D. Liu, F. Gao, Copper modified activated coke for mercury removal from coal-fired flue gas, Chem. Eng. J. 286 (2016) 585–593.
[25] Y. Xie, C. Li, L. Zhao, J. Zhang, G. Zeng, X. Zhang, W. Zhang, S. Tao, Experimental study on Hg0 removal from flue gas over columnar MnO_x-CeO_2/activated coke, Appl. Surf. Sci. 333 (2015) 59–67.
[26] L. Ling, M. Fan, B. Wang, R. Zhang, Application of computational chemistry in understanding the mechanisms of mercury removal technologies: a review, Environ. Sci. Technol. 8 (2015) 3109–3133.

[27] Y. Yuan, Y. Zhao, H. Li, Y. Li, X. Gao, C. Zheng, J. Zhang, Electrospun metal oxide-TiO2 nanofibers for elemental mercury removal from flue gas, J. Hazard. Mater. 227–228 (2012) 427–435.

[28] J. Liu, M.A. Cheney, F. Wu, M. Li, Effects of chemical functional groups on elemental mercury adsorption on carbonaceous surfaces, J. Hazard. Mater. 186 (2011) 108–113.

[29] T.A. Baghemiyani, F. Kalantari Fotooh, Interaction of lead metal with single walled AlN nanotube: a computational study, J. Inorg. Organomet. Polym. Mater. 27 (2017) 1274–1280.

[30] Z. Gao, W. Yang, Effects of CO/CO_2/NO on elemental lead adsorption on carbonaceous surfaces, J. Mol. Model. 22 (2016) 166.

[31] P. Blowers, B.G. Kim, The adsorption of mercury-species on relaxed and rumpled CaO (0 0 1) surfaces investigated by density functional theory, J. Mol. Model. 17 (2011) 505–514.

[32] G. Xin, P. Zhao, C. Zheng, Theoretical study of different speciation of mercury adsorption on CaO (001) surface, Proc. Combust. Inst. 32 (2009) 2693–2699.

[33] P. Xue, Z. Fu, Z. Yang, The density functional theory studies on the promoting effect of the Cu-modified Fe_3O_4 catalysts, Phys. Lett. A 379 (2015) 607–612.

[34] L. Tao, X. Guo, C. Zheng, Density functional study of Hg adsorption mechanisms on α-Fe_2O_3 with H_2S, Proc. Combust. Inst. 34 (2013) 2803–2810.

[35] P. Guo, X. Guo, C.-G. Zheng, Computational insights into interactions between Hg species and α-Fe_2O_3(001), Fuel 90 (2011) 1840–1846.

[36] X. Wang, Y. Huang, Z. Pan, Y. Wang, C. Liu, Theoretical investigation of lead vapor adsorption on kaolinite surfaces with DFT calculations, J. Hazard. Mater. 295 (2015) 43–54.

[37] Y. Gao, Z. Li, A DFT study of the Hg^0 oxidation mechanism on the V_2O_5-TiO_2(001) surface, Mol. Catal. 433 (2017) 372–382.

[38] Z. Wang, J. Liu, B. Zhang, Y. Yang, Z. Zhang, S. Miao, Mechanism of heterogeneous mercury oxidation by HBr over V_2O_5/TiO_2 catalyst, Environ. Sci. Technol. 50 (2016) 5398–5404.

[39] C. Sun, C.E. Snape, H. Liu, Development of low-cost functional adsorbents for control of mercury (Hg) emissions from coal combustion, Energy Fuels 27 (2013) 3875–3882.

[40] C.-H. Chiu, Simultaneous control of elemental mercury/sulfur dioxide/nitrogen monoxide from coal-fired flue gases with metal oxide-impregnated activated carbon, Aerosol Air Qual. Res. 15 (2015) 2094–2103.

[41] Y. Zhao, R. Hao, F. Xue, Y. Feng, Simultaneous removal of multi-pollutants from flue gas by a vaporized composite absorbent, J. Hazard. Mater. 321 (2017) 500–508.

[42] Y. Zhao, R. Hao, B. Yuan, J. Jiang, Simultaneous removal of SO_2, NO and Hg^0 through an integrative process utilizing a cost-effective complex oxidant, J. Hazard. Mater. 301 (2016) 74–83.

[43] Y. Zhao, R.-L. Hao, Q. Guo, Y.-N. Feng, Simultaneous removal of SO_2 and NO by a vaporized enhanced-Fenton reagent, Fuel Process. Technol. 137 (2015) 8–15.

[44] Y. Zhao, Y. Han, T. Guo, T. Ma, Simultaneous removal of SO_2, NO and Hg^0 from flue gas by ferrate (VI) solution, Energy 67 (2014) 652–658.

[45] P. Fang, C.-P. Cen, X.-M. Wang, Z.-J. Tang, Z.-X. Tang, D.-S. Chen, Simultaneous removal of SO_2, NO and Hg^0 by wet scrubbing using urea $KMnO_4$ solution, Fuel Process. Technol. 106 (2013) 645–653.

[46] N.D. Hutson, R. Krzyzynska, R.K. Srivastava, Simultaneous removal of SO_2, NO_x, and Hg from coal flue gas using a $NaClO_2$-enhanced wet scrubber, Ind. Eng. Chem. Res. 47 (2008) 5825–5831.

[47] W. Yang, Z. Gao, X. Liu, X. Li, X. Ding, W. Yan, Single-atom iron catalyst with single-vacancy graphene-based substrate as a novel catalyst for NO oxidation: a theoretical study, Catal. Sci. Technol. 8 (2018) 10.

[48] W. Yang, Z. Gao, X. Ding, G. Lv, W. Yan, The adsorption characteristics of mercury species on single atom iron catalysts with different graphene-based substrates, Appl. Surf. Sci. 455 (2018) 940–951.

[49] Z.Y. Gao, W.J. Yang, X.L. Ding, G. Lv, W.P. Yan, Support effects on adsorption and catalytic activation of O_2 in single atom iron catalysts with graphene-based substrates, Phys. Chem. Chem. Phys. 20 (2018) 7333–7341.

[50] Z. Gao, W. Yang, X. Ding, G. Lv, W. Yan, Support effects in single atom iron catalysts on adsorption characteristics of toxic gases (NO_2, NH_3, SO_3 and H_2S), Appl. Surf. Sci. 436 (2018) 585–595.

[51] L. Jiao, G. Wan, R. Zhang, H. Zhou, S.-H. Yu, H.-L. Jiang, From metal-organic frameworks to single-atom Fe implanted N-doped porous carbons: efficient oxygen reduction in both alkaline and acidic media, Angew. Chem. 57 (2018) 8525–8529.

[52] H. Zhang, S. Hwang, M. Wang, Z. Feng, S. Karakalos, L. Luo, Z. Qiao, X. Xie, C. Wang, D. Su, Y. Shao, G. Wu, Single atomic iron catalysts for oxygen reduction in acidic media: particle size control and thermal activation, J. Am. Chem. Soc. 139 (2017) 14143–14149.

[53] X. Fang, L. Jiao, S.-H. Yu, H.-L. Jiang, Metal-organic framework-derived FeCo-N-doped hollow porous carbon nanocubes for electrocatalysis in acidic and alkaline media, ChemSusChem 10 (2017) 3019–3024.

[54] Y. Chen, S. Ji, Y. Wang, J. Dong, W. Chen, Z. Li, R. Shen, L. Zheng, Z. Zhuang, D. Wang, Y. Li, Isolated single iron atoms anchored on N-doped porous carbon as an efficient electrocatalyst for the oxygen reduction reaction, Angew. Chem. 129 (2017) 7041–7045.

[55] Z.B. Liang, C. Qu, D.G. Xia, R.Q. Zou, Q. Xu, Atomically dispersed metal sites in MOF-based materials for electrocatalytic and photocatalytic energy conversion, Angew. Chem. 57 (2018) 9604–9633.

[56] Y. Han, Y. Wang, R. Xu, W. Chen, L. Zheng, A. Han, Y. Zhu, J. Zhang, H. Zhang, J. Luo, Electronic structure engineering to boost oxygen reduction activity by controlling the coordination of the central metal, Energy Environ. Sci. 11 (2018) 2348–2352.

[57] Z. Gao, M. Li, Y. Sun, W. Yang, Effects of oxygen functional complexes on arsenic adsorption over carbonaceous surface, J. Hazard. Mater. 360 (2018) 436–444.

[58] G. Kresse, D. Joubert, From ultrasoft pseudopotentials to the projector augmented-wave method, Phys. Rev. B 59 (1999) 1758.

[59] J.P. Perdew, K. Burke, M. Ernzerhof, Generalized gradient approximation made simple, Phys. Rev. Lett. 77 (1996) 3865.

[60] G. Kresse, J. Furthmüller, Efficiency of ab-initio total energy calculations for metals and semiconductors using a plane-wave basis set, Comput. Mater. Sci. 6 (1996) 15–50.

[61] G. Kresse, J. Furthmüller, Efficient iterative schemes for ab initio total-energy calculations using a plane-wave basis set, Phys. Rev. B 54 (1996) 11169.

[62] S. Grimme, J. Antony, S. Ehrlich, H. Krieg, A consistent and accurate ab initio parametrization of density functional dispersion correction (DFT-D) for the 94 elements H-Pu, J. Chem. Phys. 132 (2010) 154104.

[63] Z. Gao, Y. Sun, M. Li, W. Yang, X. Ding, Adsorption sensitivity of Fe decorated different graphene supports toward toxic gas molecules (CO and NO), Appl. Surf. Sci. 456 (2018) 351–359.

[64] M. Manadé, F. Viñes, F. Illas, Transition metal adatoms on graphene: a systematic density functional study, Carbon 95 (2015) 525–534.

[65] P. Janthon, S.M. Kozlov, F. Vines, J. Limtrakul, F. Illas, Establishing the accuracy of broadly used density functionals in describing bulk properties of transition metals, J. Chem. Theory Comput. 9 (2013) 1631–1640.

[66] A.V. Krasheninnikov, P.O. Lehtinen, A.S. Foster, P. Pyykko, R.M. Nieminen, Embedding transition-metal atoms in graphene: structure, bonding, and magnetism, Phys. Rev. Lett. 102 (2009) 126807.

[67] Y. Tang, J. Zhou, Z. Shen, W. Chen, C. Li, X. Dai, High catalytic activity for CO oxidation on single Fe atom stabilized in graphene vacancies, RSC Adv. 6 (2016) 93985–93996.

[68] S. Kattel, P. Atanassov, B. Kiefer, Stability, electronic and magnetic properties of in-plane defects in graphene: a first-principles study, J. Phys. Chem. C 116 (2012) 8161–8166.

[69] A.T. Lee, J. Kang, S.-H. Wei, K.J. Chang, Y.-H. Kim, Carrier-mediated long-range ferromagnetism in electron-doped Fe-C4 and Fe-N4 incorporated graphene, Phys. Rev. B 86 (2012) 165403.

[70] P.A. Denis, F. Iribarne, Comparative study of defect reactivity in graphene, J. Phys. Chem. C 117 (2013) 19048–19055.

[71] G.C.A. da Hora, R.L. Longo, J.B.P. da Silva, Calculations of structures and reaction energy profiles of As_2O_3 and As_4O_6 species by quantum chemical methods, Int. J. Quantum Chem. 112 (2012) 3320–3324.

[72] Z.J. Wu, Theoretical study on PbS, PbO and their anions, Chem. Phys. Lett. 370 (2003) 39–43.

[73] M. Benavides-Garcia, K. Balasubramanian, Bond energies, ionization potentials, and the singlet–triplet energy separations of $SnCl_2$, SnBr 2, Sn_I2, PbC_l2, PbB_r2, Pb_I2, and their positive ions, J. Chem. Phys. 100 (1994) 2821–2830.

[74] Q. Luo, W. Zhang, C.-F. Fu, J. Yang, Single Pd atom and Pd dimer embedded graphene catalyzed formic acid dehydrogenation: a first-principles study, Int. J. Hydrogen Energy 43 (2018) 6997–7006.

[75] Y. Li, H. Su, S.H. Chan, Q. Sun, CO_2 electroreduction performance of transition metal dimers supported on graphene: a theoretical study, ACS Catal. 5 (2015) 6658–6664.

[76] Z. He, K. He, A.W. Robertson, A.I. Kirkland, D. Kim, J. Ihm, E. Yoon, G.-D. Lee, J.H. Warner, Atomic structure and dynamics of metal dopant pairs in graphene, Nano Lett. 14 (2014) 3766–3772.

[77] E. Clementi, D.L. Raimondi, W.P. Reinhardt, Atomic screening constants from SCF functions. II. Atoms with 37 to 86 electrons, J. Chem. Phys. 47 (1967) 1300–1307.

[78] Y. Tang, Z. Liu, Z. Shen, W. Chen, D. Ma, X. Dai, Adsorption sensitivity of metal atom decorated bilayer graphene toward toxic gas molecules (CO, NO, SO_2 and HCN), Sens. Actuators, B 238 (2017) 182–195.

[79] B. Huang, L. Xiao, J. Lu, L. Zhuang, Spatially resolved quantification of the surface reactivity of solid catalysts, Angew. Chem. 55 (2016) 6239–6243.